2013

Biophotonic logic devices based on quantum dots and temporally-staggered Forster energy transfer relays

Jonathan C. Claussen
W. Russ Algar, *University of British Columbia*
Niko Hildebrandt
Kimihiro Susumu
Mario G. Ancona, et al.

Nanoscale

www.rsc.org/nanoscale

Volume 5 | Number 24 | 21 December 2013 | Pages 11983–12680

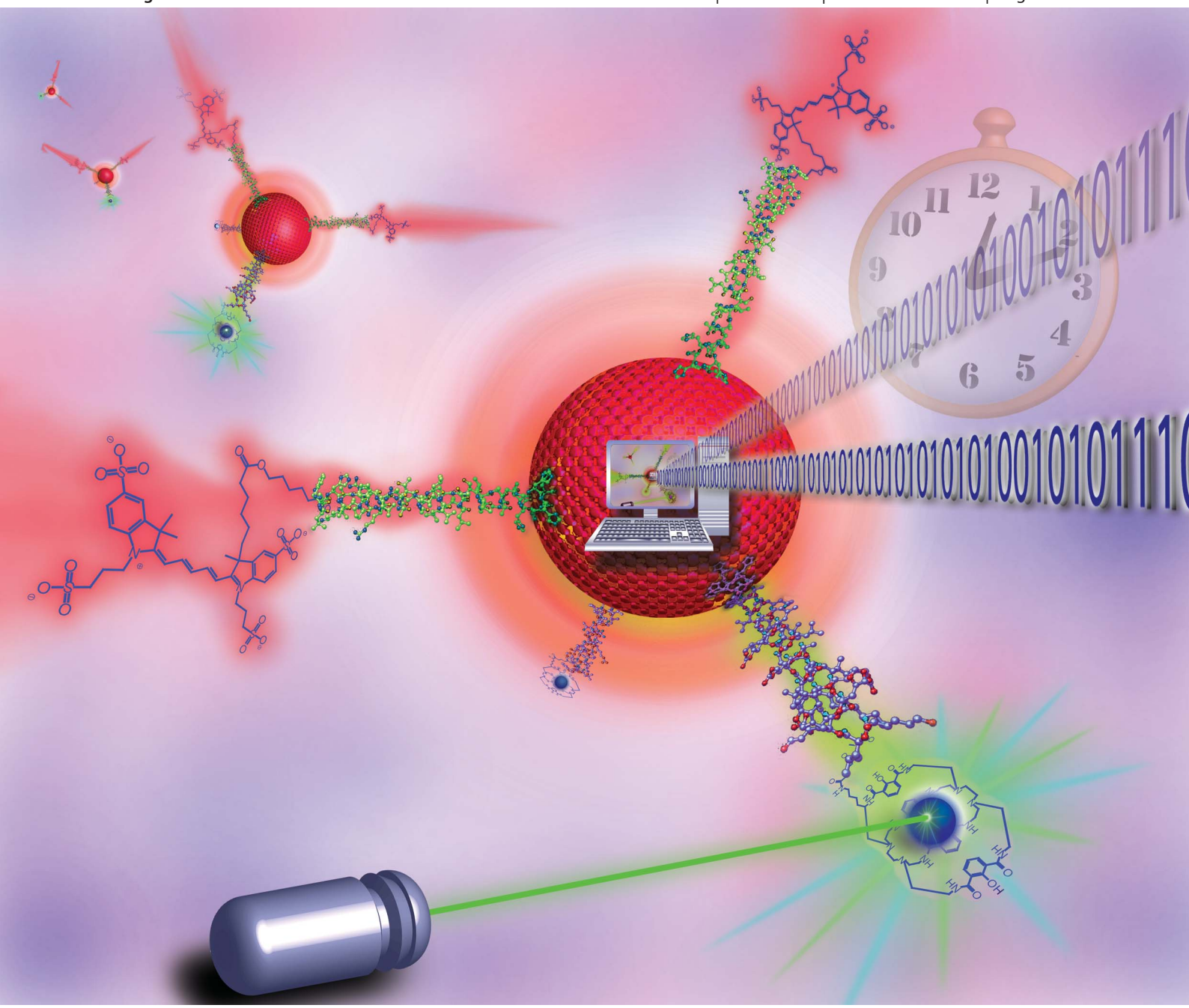

ISSN 2040-3364

PAPER

Medintz *et al.*

Biophotonic logic devices based on quantum dots and temporally-staggered Förster energy transfer relays

RSC Publishing

NCNST

2040-3364(2013)5:24;1-8

Nanoscale

RSC Publishing

PAPER

View Article Online
View Journal | View Issue

Cite this: *Nanoscale*, 2013, **5**, 12156

Biophotonic logic devices based on quantum dots and temporally-staggered Förster energy transfer relays

Jonathan C. Claussen,[ad] W. Russ Algar,[e] Niko Hildebrandt,[f] Kimihiro Susumu,[bg] Mario G. Ancona[c] and Igor L. Medintz*[a]

Received 16th July 2013
Accepted 19th August 2013

DOI: 10.1039/c3nr03655c

www.rsc.org/nanoscale

Integrating photonic inputs/outputs into unimolecular logic devices can provide significantly increased functional complexity and the ability to expand the repertoire of available operations. Here, we build upon a system previously utilized for biosensing to assemble and prototype several increasingly sophisticated biophotonic logic devices that function based upon multistep Förster resonance energy transfer (FRET) relays. The core system combines a central semiconductor quantum dot (QD) nanoplatform with a long-lifetime Tb complex FRET donor and a near-IR organic fluorophore acceptor; the latter acts as two unique inputs for the QD-based device. The Tb complex allows for a form of temporal memory by providing unique access to a time-delayed modality as an alternate output which significantly increases the inherent computing options. Altering the device by controlling the configuration parameters with biologically based self-assembly provides input control while monitoring changes in emission output of all participants, in both a spectral and temporal-dependent manner, gives rise to two input, single output Boolean Logic operations including OR, AND, INHIBIT, XOR, NOR, NAND, along with the possibility of gate transitions. Incorporation of an enzymatic cleavage step provides for a set-reset function that can be implemented repeatedly with the same building blocks and is demonstrated with single input, single output YES and NOT gates. Potential applications for these devices are discussed in the context of their constituent parts and the richness of available signal.

Introduction

Molecular logic devices (MLDs) that rely on biological architectures and/or bioactivity demonstrate promise for assembling non-traditional computing systems capable of nanoscale information processing.[1,2] Their unique attributes arise from the ability to create these devices out of biomolecular scaffolds (*i.e.*, proteins, peptides, nucleic acids, *etc.*) and/or biomolecular activity (*i.e.*, recognition or catalysis). Recent research has demonstrated a wide range of biocomputing activity and other targeted applications including transport/release of chemicals/drugs,[3–5] single and multi-analyte sensing,[6–9] medical diagnostics,[10–12] and nanorobotics.[13–16] Biomolecules such as single-stranded oligonucleotides (ss-DNA) and proteins (*e.g.*, enzymes) have been used to form gene-based bistable toggle switches and oscillators,[17,18] biocomputers for analyzing the content of messenger RNA to control levels of gene expression,[19] classical logic gates such as OR, AND, XOR, and INHIBIT (INH) based upon Boolean operations,[16,20–22] and arithmetic operations such as the half-adder/half-subtractor.[23–27]

Typically, MLDs are not like semiconductor-based logic in employing voltages as the input/output (I/O) signals, but instead use chemical or biochemical inputs and electrochemical[28–30] or spectroscopic/photonic outputs.[20,22,31,32] Furthermore, it is difficult to concatenate arrays of molecular logic gates into circuits since the output signal of one gate typically cannot be transduced to the input of the adjacent gate as MLD I/O signals often differ in character. Thus, MLDs have been hindered in terms of inherent complexity and function. However, recent efforts have utilized functional integration, where the MLD design incorporates a single multicomponent molecule/supramolecule (*i.e.*, unimolecular systems) to mimic complex logic circuits, and to circumvent the associated issues with limited gate-to-gate I/O transduction.[33,34] To further enhance MLD function, photonic-based MLDs (*i.e.*, I/O signals that are primarily comprised of photons) have been developed with several specific advantages over chemical, biochemical,

[a]*Center for Bio/Molecular Science and Engineering, Code 6900, USA. E-mail: Igor.medintz@nrl.navy.mil*

[b]*Optical Sciences Division, Code 5600, USA*

[c]*Electronics Science and Technology Division, U.S. Naval Research Laboratory, Code 6876, Washington, DC 20375 USA*

[d]*College of Science, George Mason University, Fairfax, VA 22030, USA*

[e]*Department of Chemistry, University of British Columbia, Vancouver, BC, V6T 1Z1 Canada*

[f]*Institut d'Electronique Fondamentale, Université Paris-Sud, 91405 Orsay Cedex, France*

[g]*Sotera Defense Solutions, Annapolis Junction, MD 20701 USA*

and electrochemical I/O signaling including: (1) photonic signaling does not create chemical byproducts that can prohibit gate cycling and lead to limited MLD life; (2) photonic input signals can be delivered remotely in rapid pulses (<1 ps) and are not bound by chemical diffusion limitations, permitting rapid gate cycling and information accumulation; (3) incident photons can penetrate individual elements of monolithic structures, permitting enhanced complexity for MLDs that use unimolecular systems; (4) a single unimolecular system comprised of multiple fluorophores can yield unique photonic outputs from the same set of inputs depending on how output PL is interpreted and converted into Boolean Logic, or by being reconfigured with changes to input wavelengths, output wavelengths, and/or chemical rearrangement of the initial state.[23,33,35,36] Combining the advantages of photonically interrogated systems with unimolecular scaffolds has much to offer for creating nanoscale devices capable of complex multi-logic operations.[16,20,22,23,31–33,35–41]

By virtue of dipole–dipole coupling between their component molecules, photonic-based MLDs often support short-range (<10 nm) internal communication *via* Förster resonance energy transfer (FRET) which opens up fruitful avenues for logic gate design.[22,42] Photonic-based MLDs utilizing FRET are well-suited for biocomputing operations due in part to their rapid response time, which permits real-time feedback; capability to detect nanoscale distances, which provides the spatial resolution necessary for monitoring minute physiochemical or cellular variations; and the ability to be genetically encoded for cellular uptake and localization to subcellular compartments, which permits locus-specific *in situ* monitoring.[43,44] FRET-based molecular logic gates are also characterized by extremely low crosstalk since the FRET rate decays as a sixth power function of the distance ($1/r^6$) separating the fluorophores; FRET crosstalk is generally eliminated as independent fluorophore-to-fluorophore distances reach >10 nm.[45]

Precise positioning of fluorophores for FRET-based molecular logic gate design continues to be quite challenging.[46] Recent strides in spacing fluorophores with nanometer precision for MLDs has been achieved with molecular beacon (MB) probes comprised of stem-loop, hairpin structured ss-DNA and switches.[47,48] Both underlying techniques require a ss-DNA strand invasion process[49] to hybridize with the fluorophore/ss-DNA/quencher array and alter the fluorophore-to-quencher distance—turning the FRET process ON or OFF and subsequently altering the output logic state. The functionality of these and other similar devices, however, continues to be significantly hampered by the photophysical properties of many of the conventional organic fluorophores that they incorporate and depend upon. Complicating issues include broad absorption and emission spectra, small Förster distances, significant direct acceptor excitation, and low quantum yields.[50–52] Furthermore, inherent Stokes shifts means that FRET-based molecular logic gates are limited to exciton transfers that are "one-way" or "downhill" in energy (*i.e.*, from blue to red) as the exciton is transferred from the excited-state donor to an acceptor fluorophore and not *vice versa*. This one-way energy flow, analogous to the current rectification of a pn diode, can severely restrict the complexity of logic gate design and the overall related (bio)computing power.[45]

As a means to partially address the restriction of "one-way" FRET and significantly enhance the complexity of available logic, we incorporate luminescent semiconductor nanocrystals or quantum dots (QD) into MLD logic design. QDs provide a host of unique photophysical properties, *e.g.*, resilience to photobleaching, high quantum yields, and a narrow photoluminescent (PL) spectra (full width at half maximum <50 nm) coupled to broad absorption profiles that increase nearly continuously to the UV; these cumulatively lend themselves directly to FRET-based nanoscale devices.[53] Such properties allow QDs to be excited at wavelengths that may be ≥100 nm away from the emission while simultaneously minimizing any direct excitation of a potential acceptor dye.[50,51] The nontrivial surface area of the nanocrystal also allows for multiple donor or acceptor molecules to be assembled around the QD in what approximates a centrosymmetric distribution. Assembling multiple acceptors around a central QD can proportionally increase the FRET acceptor absorption cross-section and hence FRET efficiency in a controllable manner, while assembling multiple donors around a central QD acceptor increases the probability that FRET will occur.[50–52,54,55]

In the present work, we exploit the unique QD FRET properties to demonstrate unimolecular biophotonic logic devices. From the perspective of digital logic, most MLDs to date[56,57] implement combinatorial logic, meaning that their output is formed directly from the values of multiple logical inputs that are presented *simultaneously*. We prototype MLDs that are capable not only of such combinatorial logic, but which can also accomplish sequential logic functions by incorporating a type of "memory" so that they can combine logical inputs that are presented at *different* times in order to form a logical output. For our MLDs, this "memory" function is supplied by luminescent terbium(III) complexes (Tb) that manifest extremely long excited-state lifetimes as a result of inherently efficient intersystem crossing. Coupling the Tb complexes with QDs and an Alexa Fluor 647 (A647) near-IR dye has previously allowed us to construct time-gated FRET relays that were applied in a number of enzymatic and DNA biosensing assays.[54,55] Evaluating the richness of distinct signals and data available within these QD-based multistep FRET systems suggested that the same configuration might directly lend itself to MLD utility. Here, we utilize the same core architecture and evaluate MLD potential by systematically controlling the number or valence of Tb and A647 conjugated to QDs. By monitoring changes in the ensemble emission both *spectrally and temporally*, we demonstrate single output logic gates including OR, AND, INH, XOR, NOR, NAND, YES, and NOT gates. The time variant nature of the PL emission found within this three-luminophore system further allows for gate transitions that lead to temporally variant NOR, NAND logic gates. We also demonstrate a set-reset function by incorporating an enzymatic cleavage step to produce YES/NO logic repeatedly with the same gates.

Results and discussion

Device architecture and function

The underlying functional architecture of the QD-based biophotonic logic device is shown schematically in Fig. 1. One of the critically enabling mechanisms underpinning this device is its use of the QD as a nanoplatform that functions both as a central assembly point and an optically active element. In the latter capacity, the QD serves not only in its standard role as a FRET donor, but also acts as a FRET acceptor, which is unusual given the QD's broad absorption, higher extinction coefficient moving towards the UV region, and long PL lifetime ($\tau \sim 10$–50 ns) as compared to most organic dyes ($\tau < 5$ ns).[50–52] The latter factors usually make the QD more favorably excited than most potential donor dyes they are paired with, and, when excited in this configuration, the QD is rendered unavailable as a ground state acceptor due to its longer excited state lifetime. However, by pairing the QD with a long-lifetime fluorophore such as a Tb complex ($\tau \sim 2.5$ ms) and an organic dye, one can observe the QD acting both as an acceptor (for the Tb) and as a donor (for the A647) during the temporal evolution of the system. In practice, when the QD is paired with neither Tb nor A647 (Fig. 1a), a sole emission peak at 625 nm (blue spectrum) is noted when monitoring PL nearly immediately after an UV excitation pulse (*i.e.*, no time delay). Pairing the QD with both Tb and A647, as shown in Fig. 1b, followed by immediate excitation/monitoring allows the QD to act as a donor to sensitize the A647 (blue spectrum). As the QD and A647 relax with time, the Tb is then able to sensitize the QD, which becomes available as an acceptor. In turn, the QD functions as an intermediary donor, relaying the energy to the A647. Time-delayed PL monitoring provides a composite emission of the initial Tb donor, the Tb-sensitized QD, and the Tb-QD-sensitized A647 (orange spectrum). Critically, initial Tb and Tb-to-QD sensitization are not apparent in any spectra unless appropriate time delays are used in the spectral data collection. Furthermore, although the possibility exists for Tb → A647 FRET ($R_0 \sim 5.7$ nm), see Fig. 1c-d, this pathway is unfavored due to the much faster Tb → QD ($R_0 \sim 10.1$ nm) and QD → A647 ($R_0 \sim 7.5$ nm) FRET rates, which are estimated to be 30× and 5× faster, respectively, at the expected separation distances in the construct.[54] Indeed, the almost non-existant impact of this putative FRET process has been confirmed experimentally.[54] Pertinent fluorophore photophysical and FRET donor/acceptor properties are provided in the Experimental Section.

It is critical to note that our QD-based logic devices all have 2 distinct and variable inputs, namely the Tb and the A647 dye; these are controllably assembled to the central QD, see Fig. 1. This allows the construct to function as a two input, single output

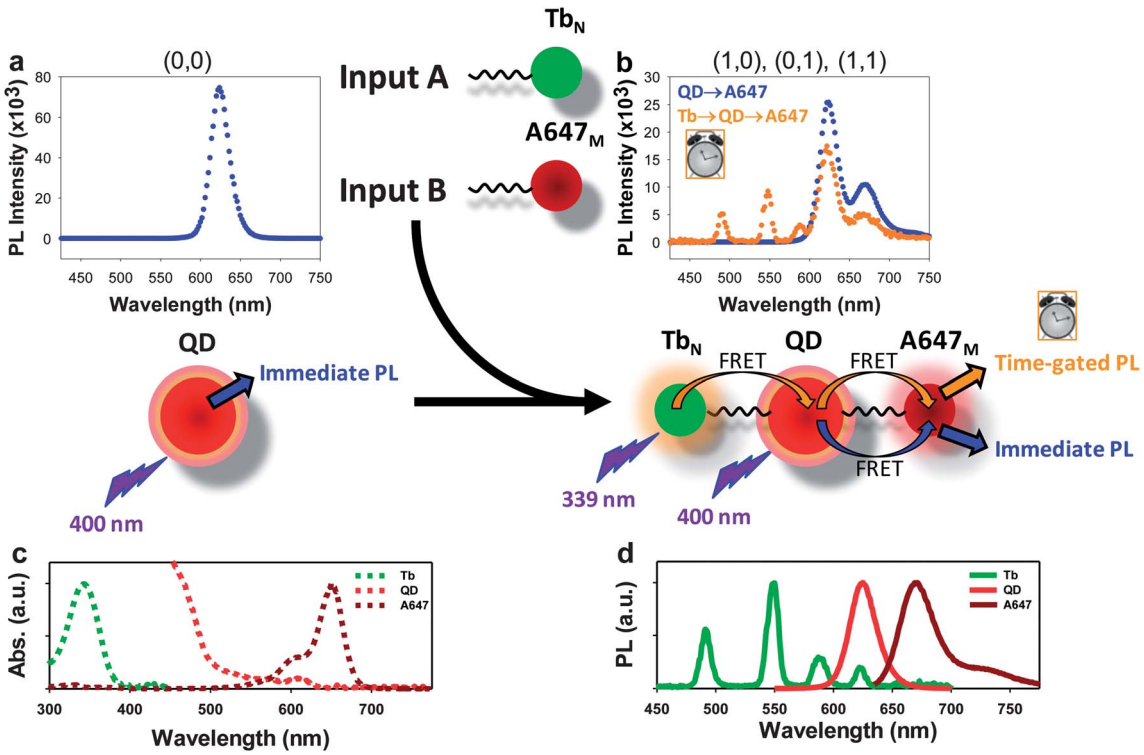

Fig. 1 Two input, single output photonic logic gate schematic of the Tb-QD-A647 three-fluorophore system with four input states where the (a) initial input state (0,0) contains QD with no Input *A* (A647) nor Input *B* (Tb). The (b) subsequent states ((0,1), (1,0), (1,1)) contain distinct valences of Input *A* and Input *B*. Inset photoluminescence (PL) plots display the output PL intensity immediately (blue plot) and 55 μs (orange plot) after UV excitation. QD peak PL ~625 nm; Tb peaks at ~490, 550, 585, and 620; A647 peak PL ~670 nm. Note, the contribution of the Tb peak at 620 nm to the QD peak at 625 nm is deconvolved and accounted for in all logic gates. Immediate PL monitoring (blue) results in (a) either direct QD PL or in (b) QD-A647 FRET and emission from both. Time-delayed PL monitoring (orange – indicated by the clock) results in a convolution of Tb, QD, and A647 PL (b). Changing the valence of Tb_N- or $A647_M$ per QD provides for control over the magnitude, and to some extent influence, of these inputs on device emission. For time-gated monitoring, the Tb is preferentially excited at 339 nm while for immediate PL monitoring the QD is excited at 400 nm which excludes the Tb. Normalized absorption (c) and emission (d) spectra for the Tb, QD and A647.

photonic logic gate with four input states based on *the presence and ratio* of Tb and A647 attached per QD. This combination alters both the immediate and time-delayed spectra to produce 4 distinct logic states as shown in Fig. 1a: QD and no Tb nor A647, defined here as (0,0); (Fig. 1b) QD and N Tb and M A647 (1,0), (0,1), (1,1). The Tb provides access to the time-delayed domain and acts to sensitize the QD in that domain, while the A647 acts as a terminal acceptor and alters the PL ratios in the construct both in an immediate and time-gated manner. In the following examples, all constructs have the 2 inputs and in most cases both are varied to produce distinct logic operations. Thus the bulk of the logic gates demonstrated here manifest inherently *digital* and not analog operations, although we also demonstrate other types of logic devices as well. An alternative logic scenario where both Tb and A647 inputs are joined to act as a single input while distinct time points act as the variable inputs is shown in Fig. 5. This type of *sequential* logic demonstrates how temporally variant PL can change the assessed logical operations. Simplified single input, single output logic gates that can undergo continuous chemical regeneration are also highlighted.

Assembly of the QD-based photonic logic devices follows our previous fabrication protocol.[54,55] The second critical factor enabling the function of these devices is the ability to assemble polyhistidine (His_n)-appended peptides to QDs *via* metal affinity coordination in a carefully controlled and *ratiometric* manner. His_n-peptides spontaneously coordinate onto the Zn^{2+}-rich QD surface with high affinity ($K_d^{-1} \sim 10^9\ M^{-1}$) in a variety of buffers and in a facile manner that only requires mixing of molar ratios of the two reactants.[58–60] We have determined that smaller 530 nm emitting QDs (diameter ~6 nm) can display on average a ratio of 50 ± 10 such peptides/QD; the larger 625 nm QDs used here (diameter ~10 nm, surface functionalized with PEG-appended dihydrolipoic acid)[54,55] can accommodate a far higher surface valence of peptide.[61] The systems described below utilize self-assembling His_6-appended peptides prelabeled with each fluorophore; these peptides are designated as PEP A-A647 and PEP B-Tb, respectively. The sequences and labeling procedure are described in the Experimental Section. Use of these peptides for QD assembly allows the respective labels to be ratiometrically displayed at relatively fixed centrosymmetric distances from the central QD.[51,58–61]

Photophysical characterization

To determine the photophysical boundaries that would characterize the QD-FRET logic devices, we began by performing an initial baseline characterization of QD → A647, Tb → QD, and Tb → QD → A647 FRET. For this purpose, ratios of 4, 12 and 25 Tb-labeled peptide/QD were used while the valence of A647/QD was incrementally raised in a stepwise manner from 0 to 25 within each construct. The resulting spectra collected with both immediate (left panel) and time-gating (right panel) are shown in Fig. 2a–c. The first FRET process between the central QD and an adjacent A647 dye is observed immediately following 400 nm UV excitation as emission spectra appear at approximately 625 nm and 670 nm corresponding to peak PL emissions of the QD and A647 respectively (Fig. 2a–c, left column). To produce Tb-based PL spectra and isolate signal from the second FRET process (*i.e.*, Tb-QD FRET), the Tb was preferentially excited at 339 nm and a time delay of 55 μs with an integration time of 1 ms was utilized. These parameters were chosen empirically to ensure ample time for dissipation of emission signal resulting from direct excitation of the QD and to ensure proper collection of Tb PL spectra.[54,62] After said time delay, sharp emission lines appear at approximately 490 nm, 550 nm, 585 nm, 625 nm, and 670 nm corresponding to peak PL emissions from Tb, QD, and A647, respectively (Fig. 1a–c, right column). The peak QD PL emission line (625 nm) decreases as the number or valence of A647 dye displayed around it increases and, concomitantly, the QD-A647 FRET efficiency increases in both the immediate and time-delayed mode. For all data acquired immediately after UV excitation, the QD → A647 FRET spectra look essentially the same (compare Fig. 2a–c left panel) confirming that Tb presence does not impinge upon their emission within this collection mode. Control samples confirmed that there was no significant Tb → A647 FRET (data not shown). The direct excitation of A647 at these wavelengths is <5%, which, in combination with the use of time gating (where appropriate), avoids any significant contribution or complication in the logic system. The resultant peak PL intensity ratios observed for A647 (670 nm)/QD (625 nm), termed Output A, and A647 (670 nm)/Tb (550 nm), termed Output B, collected in immediate and time-delayed fashion, respectively, are employed as the defining logic gate output; 670 nm and 550 nm are the dominant emission peaks associated with A647 and Tb emission, respectively. Here, ratio values greater than 1 for the 670 nm/625 nm ratio (Output A, immediate) and greater than 0.5 for the 670 nm/550 nm ratio (Output B, time-delayed) are interpreted as the respective Boolean Logic state of "ON" or "1" while values below 1 and 0.5, respectively, are interpreted as an "OFF" or "0" (Fig. 2d). The distinct parabolic nature of the latter time delay PL ratio plots as opposed to the linear nature of the prompt PL ratio plot (Fig. 2d) opens the door for the formation of different photonic logic gates. For example, logic that requires output signals that have both an OFF ground state (when both inputs are not present) and OFF double input state (when both inputs are present) such as the INHIBIT and XOR gate could potentially be created with the parabolic ratio plot but not with the linear plot.[56,57] Thus, logic gates that are clearly distinct from each other can be fabricated by altering both the valence of A647 and Tb around the universal QD component, and by changing the time at which the output PL intensity is monitored.

Logic gates: OR and AND

We next evaluated the potential of this photonic assembly for creating different types of logic gates by changing the ratios of dye-labeled peptide inputs along with how the resulting PL spectra were interrogated. The first set of QD-based logic gates (*i.e.*, OR, AND, INH, and XOR) that were constructed each had a ground state (0,0) of "OFF" or "0" that consisted of QD alone, see Fig. 3 & 4. The molecular construction of the QD-based OR and AND logic gates are schematically portrayed in Fig. 3a and d, respectively. The OR logic gate verifies the presence of any input and accordingly

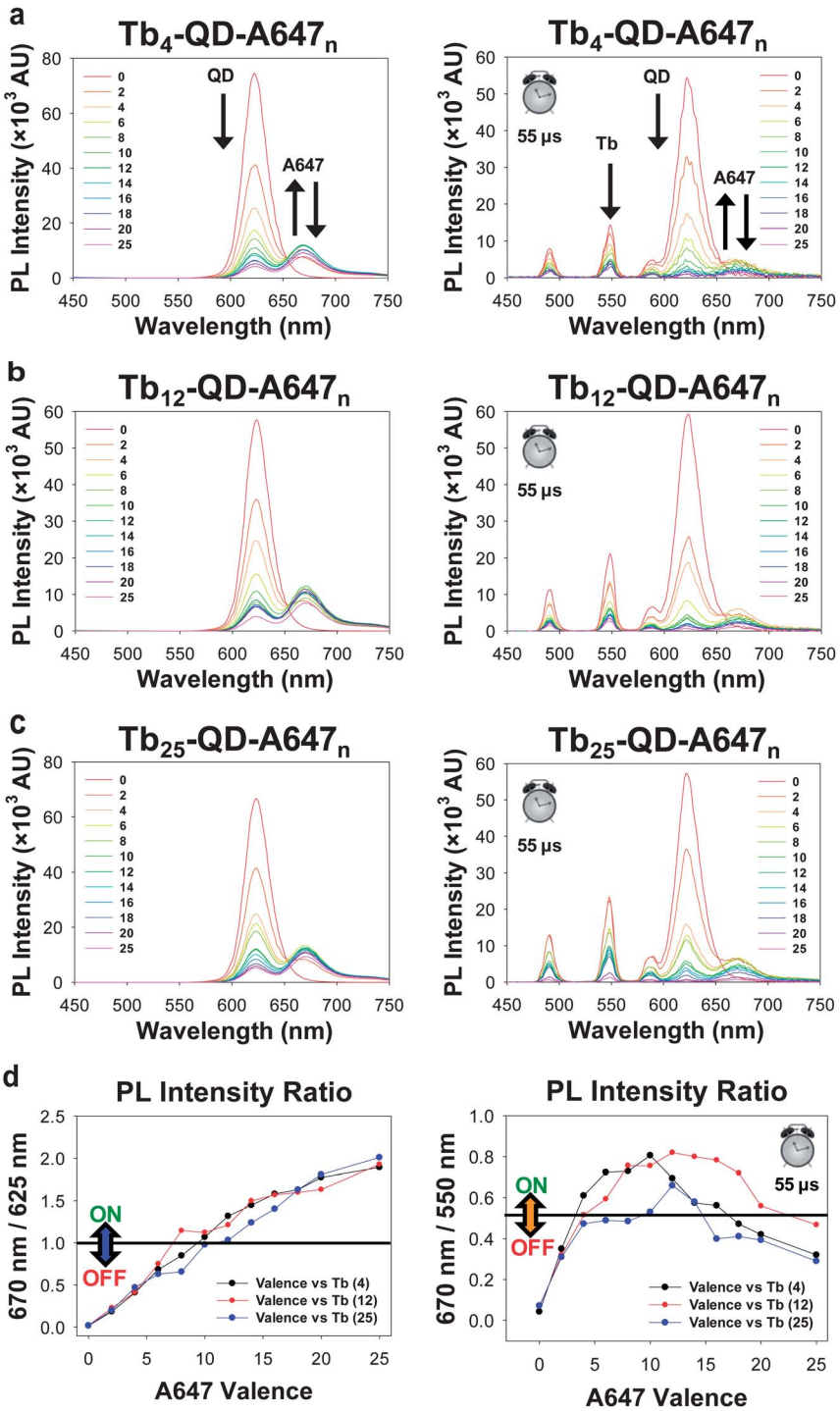

Fig. 2 The complete spectra for Tb-QD-A647 conjugates where the valence of A647 assembled per QD is varied from 0 to 25 (see graph insets) and the valence of Tb assembled per QD is fixed at 4 (a), 12 (b), and 25 (c), respectively. Acquisition time after UV 400 nm excitation is immediate (left) or utilizes 339 nm with 55 µs time delay (right). The resultant peak PL intensity ratios of A647 (670 nm)/QD (625 nm) and A647 (670 nm)/Tb (550 nm) observed (d, left) immediately and (d, right) 55 µs after UV excitation, respectively. These can be assigned Boolean Logic states "ON"/"OFF" for threshold values greater/less than 1 for the 670 nm/625 nm ratio (Output A) and greater/less than 0.5 for the 670 nm/550 nm ratio (Output B). See Experimental for the relevant photophysical characteristics that correspond to the individual fluorophore and FRET gate outputs. Arrows in (a) indicated trends in PL following the changes in A647/QD ratio either with immediate or time-gated observation.

produces an output of "1" when at least one input is "1" (Fig. 3c). PL intensity ratios of 670 nm/625 nm acquired with 400 nm UV excitation (Output A – no delay) and 670 nm/550 nm acquired 55 µs after 339 nm UV excitation (Output B – time delay) are used as outputs in the creation of both these logic gates (Fig. 3b and e). The corresponding AND gate acts as a carry digit in Boolean logic and produces an output of "1" only when both inputs are "1" (Fig. 3d–f). The OR logic gate demonstrated here can be created

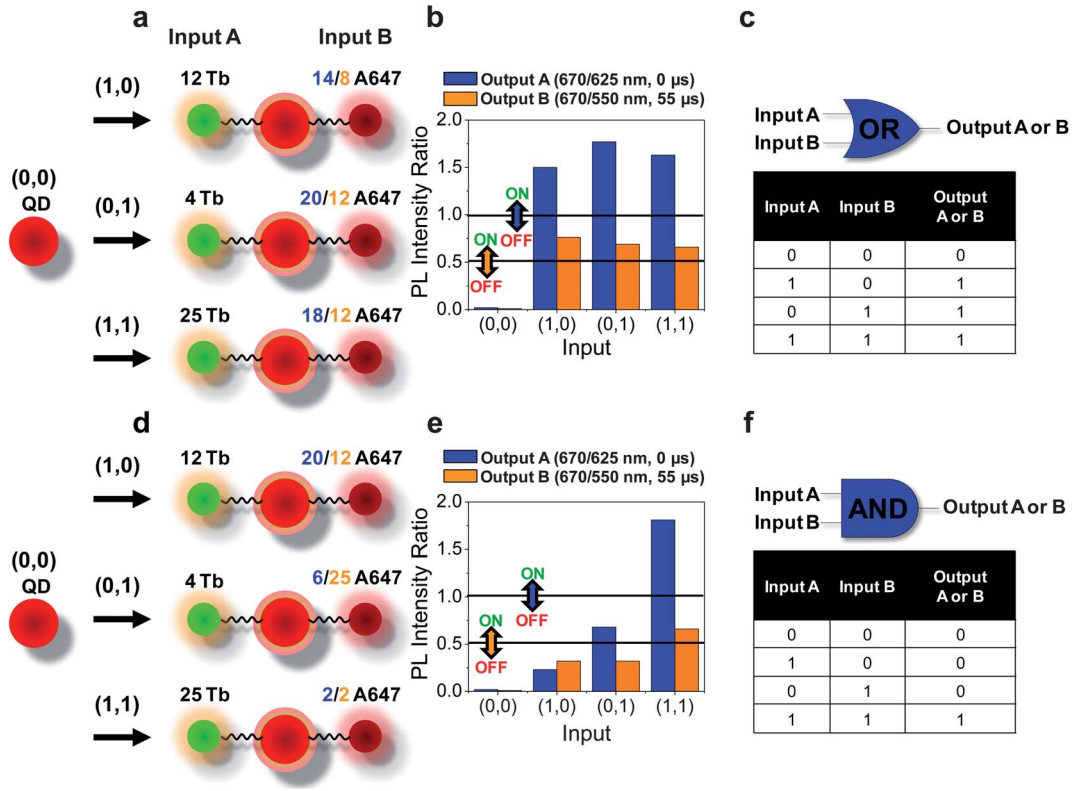

Fig. 3 Two input molecular photonic OR and AND gates highlighting the ability to create the logic gates with either the use of immediate (Output A) or time-gated (Output B) monitoring. (a) For the OR logic gate functioning with an immediate output (0 μs – no time delay) configuration, the QD is assembled with Input *A* and Input *B*: (0,0) QD alone; (1,0) QD with 12 Tb and 14 A647; (0,1) QD with 4 Tb and 20 A647; and (1,1) QD with 25 Tb and 18 A647. For the OR logic gate functioning with a time delay output (55 μs) configuration, the QD is assembled with the same Input *A* Tb ratios while Input *B* A647 ratios are varied between 8 and 12. The difference in A647 valence/QD used between immediate and time-gated is shown under Input *B* with blue and orange values/A647, respectively. (b) The OR gate fluorescence output acquired immediately (Output A, blue) and with time delay (Output B, orange): the peak PL intensity ratio of the A647 (670 nm) and the QD (625 nm) acquired (blue) immediately after UV excitation (400 nm) and the ratio of A647 (670 nm) and the Tb (550 nm) acquired (orange) at 55 μs after 339 nm UV excitation. The ratios above 1 and 0.5, for immediate and time-gated monitoring, respectively, are converted into the Boolean Logic state of "ON or 1" and ratios below 1 and 0.5 are "OFF or 0". (c) The OR logic gate schematic and corresponding truth table. Configuration for the AND gate assembly functioning in a similar manner (d) along with the corresponding fluorescence output (e) and logic gate schematic with corresponding truth table (f).

with an immediate monitoring modality by collecting PL (blue) following the conjugation of 12, 4, and 25 Tb-peptides around a central QD and then adding 14, 20, or 18 A647 dye-labeled peptides to each, respectively, to produce Input *A* (1,0), Input *B* (0,1), and Input *A* + *B* (1,1) for Output A, respectively. Highlighting the modularity of this system, the OR logic can also be created with PL collected in a time-delayed fashion (orange) by conjugating 12, 4, and 25 Tb-peptides around a central QD and then adding 8, 12, or 12 A647 dye-labeled peptides which are the representative inputs for Output B. Likewise the AND logic gate can be created with immediate and time-delayed PL by conjugating 12, 4, and 25 Tb-peptides around a central QD and then adding either 20, 6, or 2 A647 dyes or 12, 25, or 2 A647 dyes, respectively, to produce Input *A* (1,0), Input *B* (0,1), and Input *A* + *B* (1,1).

Logic gates: XOR and INHIBIT

The set of XOR and INH logic gates shown in Fig. 4 were developed following similar design protocols to the OR and AND gates above, however, all fluorescent emission is now only monitored with 55 μs time delay (*i.e.*, Output B above). As with the previous, the ground state (0,0) for both the XOR and INH gates consisted of QD alone. The INH gate, which contains a particular combination of AND and NOT logic, behaves non-commutatively as opposed to the commutative OR, AND, and XOR gates.[66,67] The INH gate produces an output of "1" only when one input is present and the other is absent; that is, Input *A* and Input *B*, respectively, in this example (Fig. 4c). The XOR gate acts as a comparator as it establishes whether two inputs have the same value and therefore produces an output of "1" when one and only one input is "1" and the other input is "0" (Fig. 4f). The realization of a XOR logic gate at the molecular level has proven to be challenging as both the ground state (0,0) and Input *A* + *B* (1,1) state need to be "OFF", or in terms of classical electrical circuitry, an XOR gate contains two bipolar switches.[63] The realization of XOR photonic logic has typically involved complex initial conditions including: dye irradiation/excitation at multiple wavelengths,[64] conformational changes in hairpin DNA probes,[48] and threading/unthreading of molecular machines.[65] In this work, such complex initial conditions are circumvented by adding access to a single external variable to the system, namely time.

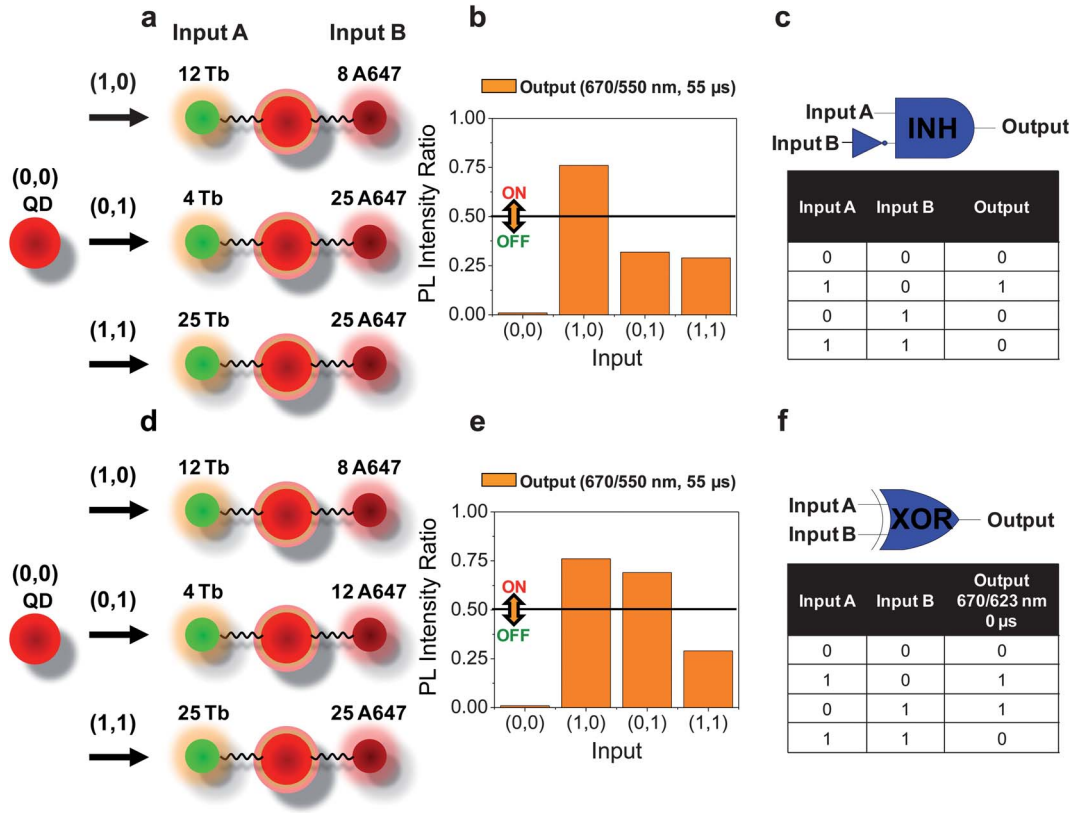

Fig. 4 Two input molecular photonic INHIBIT (INH) and XOR gates acquired in a time delay fashion. (a) For the INH logic gate, the QD is assembled with Input *A* and Input *B*: (0,0) QD alone; (1,0) QD with 12 Tb and 8 A647; (0,1) QD with 4 Tb and 25 A647; and (1,1) QD with 25 Tb and 25 A647. (b) The INH gate fluorescence output where the peak PL intensity ratio (A647 (670 nm)/Tb (550 nm)) above 0.5 acquired at 55 μs after 339 nm UV excitation is converted into the Boolean Logic state of "ON or 1" and the ratio below 0.5 is "OFF or 0". (c) The INH logic gate schematic and corresponding truth table. Configuration for the XOR gate assembly functioning in a similar manner (d) along with the corresponding fluorescence output (e) and logic gate schematic with corresponding truth table (f).

The QD-based INH logic gate is created by conjugating 12, 4, and 25 Tb around a central QD and then adding 8, 25, or 25 A647 dyes to produce Input *A* (1,0), Input *B* (0,1), and Input *A* + *B* (1,1) respectively, see Fig. 4a–c. The time-delayed Tb-sensitization of the QDs permits an incremental amplification of the Tb and QD PL that corresponds with a decrease in A647 emission as its display valency around the QD increases (Fig. 2). This particular type of emission pattern is partially attributable to the fact that each potential QD donor can only engage in FRET with one A647 acceptor at a time and the complex underlying energy transfer mechanisms of this system.[54,55] Thus an "OFF" output emission can be registered at the (0,0) ground state where no A647 dyes are present and at the (1,1) additive input state where the valence of A647 and Tb to QD is high. The QD-based XOR logic gate presented in this work is formed by conjugating 12, 4, and 25 Tb around a central QD and then adding 8, 12, or 25 A647 dyes to produce Input *A* (1,0), Input *B* (0,1), and Input *A* + *B* (1,1) respectively, see Fig. 4d–f.

Logic gates: NOR and NAND with gate transitioning

We next sought to access the rich information available within these complexes by prototyping a slightly different system. Here, in contrast to the previous configurations, we attempt to evaluate time as the variable inputs while holding constant the valence of Tb and A647 to QD. This approach significantly increases the complexity available to this QD-based photonic logic device and allows us to integrate a gate transition (GT) with NOR and NAND gate functions. The GT in a logic circuit is typically defined as the point where a switch occurs between two different stable states in response to a change of the input signal. The two input and single output logic gates of NOR and NAND can be created by considering the switching of the Boolean Logic state around the GT line. The NOR and NAND gates produce the inverted results of the OR and AND gates and accordingly require an output of "1" or "ON" at the (0,0) initial ground state. Thus the NOR and NAND logic gates cannot be created by monitoring the change in A647/QD ratio (Output A) as the PL intensity ratios *versus* A647 valence produce initial ground states (0,0) that are always 0 or "OFF" as previously mentioned. However, the NOR and NAND gates can be created by monitoring the Output B PL intensity ratio (*i.e.*, the A647/Tb ratio) at a distinct time where the Boolean Logic State is "ON" before and at the GT, and "OFF" after the GT (Fig. 5). For these prototyping purposes, we excite the system with 339 nm UV excitation and again use 670 nm for monitoring the A647 PL but switch to the 585 nm line for monitoring Tb PL.

To implement this, the PL intensity profiles for Tb-QD-A647 constructs (*i.e.*, 12 Tb and varying valences of A647 dyes conjugated to a central QD) were analyzed over a distinct set of incremental time delays from 10 to 100 μs to elucidate the

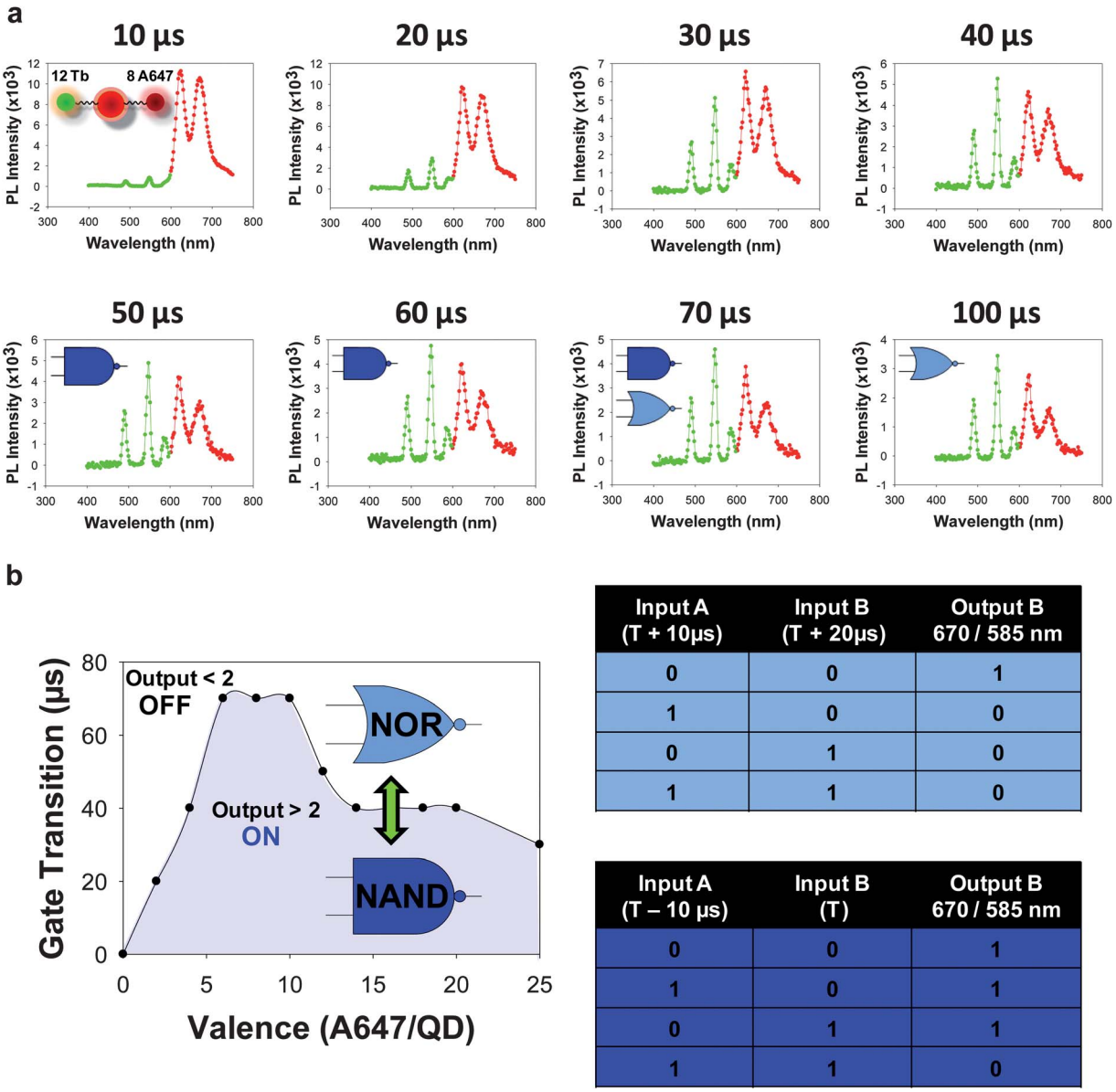

Input A (T + 10µs)	Input B (T + 20µs)	Output B 670 / 585 nm
0	0	1
1	0	0
0	1	0
1	1	0

Input A (T – 10 µs)	Input B (T)	Output B 670 / 585 nm
0	0	1
1	0	1
0	1	1
1	1	0

Fig. 5 (a) Representative PL spectra for Tb-QD-A647 conjugates at distinct time lags (10–100 µs) where the valence of A647 and Tb is fixed at 8 and 12, respectively. Inset in the first plot diagrams the Tb-QD-A647 conjugates with the Tb complexes as green spheres, A647 dye as small red spheres, and the QD as the central, large red sphere. The PL spectral points are portrayed in split color: the green portion of the plot represents PL from Tb emission with red for the QD and A647 emission. NOR and NAND states are shown schematically where they would be present in this configuration. (b) Graph displaying the Gate Transition (GT) time or time lag after UV pulse excitation (339 nm) of Tb-QD-A647 constructs (*i.e.*, 12 Tb complexes and varying ratios of A647 dyes conjugated to a single, central QD) where the peak PL intensity ratio [A647 (670 nm)/Tb complex (585 nm) – Output B] transitions from a value of greater than 2 to less than 2. The ratio above 2, values below the Gate Transition (GT) line (highlighted in blue), are converted into the Boolean Logic state of "ON or 1" and ratios below 2, values above the Gate Transition (GT) line (white), are "OFF or 0". Time-controlled, two input molecular photonic "NAND" and "NOR" gates are created from the Boolean Logic states before, at, or after the GT line. The "NOR" gate truth table (light blue) contains the following time lag states for Input *A* and Input *B*: (0,0) no time lag; (1,0) time lag of 10 µs after PL collection time measured from excitation (*T*); (0,1) time lag of 20 µs after *T*; and (1,1) time lag summing (*T* + 10 µs) and (*T* + 20 µs). The "NAND" gate truth table (dark blue) contains the following time lag states for Input *A* and Input *B*: (0,0) no time lag; (1,0) time lag of 10 µs before PL collection time measured from excitation (*T*); (0,1) time lag corresponding to *T*; and (1,1) time lag summing (*T* – 10 µs) and (*T* time).

transient PL signal intensity profiles associated with time-delayed Tb-sensitization of the QDs. Fig. 5a displays such a representative example of PL spectra collected temporally from a QD sample displaying the aforementioned 12 Tb-labeled peptides and a ratio of 8 A647-labeled peptides. Photophysical analysis of the resulting emission profile at 10 µs increments reveals spectra again associated with residual PL signal from the QD and A647 appearing at approximately 625 nm and 670 nm, respectively (Fig. 5a, red colored spectrum). Such emission lines correspond to the very strong direct 339 nm excitation of the QDs and subsequent FRET from QD to A647. Emission lines also begin to appear at 490 nm and 550 nm, corresponding to emission from the long-lived excited state of Tb (Fig. 5a, green colored spectrum). At 20 µs, the Tb associated

emission line of 585 nm becomes more distinguishable as the peak emission at 490 nm and 550 nm intensifies. Emission peaks at 625 nm and 670 nm continue to quench as initial QD excitation energy transfers and subsequently emits *via* the A647 through FRET. Despite QD "recharging" by Tb-sensitized FRET, emission peaks at 625 nm and 670 nm continue to quench with increasing time and indirect energy transfer *via* QD-A647 FRET putatively dominates the Tb-QD-A647 energy balance. However, the Tb associated emission peaks (*i.e.*, 490 nm, 550 nm, and 585 nm) continue to intensify until a maximum is reached at approximately 50 μs within this instrumental configuration.

These progressive PL signal intensity plots enable the extraction of unique PL spectral profiles from a single Tb-QD-A647 system as a function of time, leading to distinct logic outputs from identical initial logic stimuli. As the Tb-sensitized FRET to QD temporally undergoes a complex process of transitioning from residual signal from directly excited QD-to-A647 FRET to signal from the Tb-QD-A647 process, the 670 nm/585 nm (defined as Output B for these purposes) peak emission ratios change as a function of A647 valence. Thus, the initial Output B ratios start out high (*i.e.*, $\gg 2$) as A647 (670 nm) emission peaks are large compared to the representative Tb emission peak (585 nm). The Output B ratios eventually become low (*i.e.*, <2) as the Tb 585 nm emission peak intensifies and the 670 nm peak shows progressive quenching. The time in which Output B changes from high to low is plotted as the GT *versus* the A647 valence, see Fig. 5b. The GT increases as the valence of A647 increases; the 670 nm emission peak intensifies with increasing numbers of A647 and then begins to reverse itself as the valence of A647 exceeds 10. The NOR and NAND gates are thus stipulated by the switching of the Boolean Logic state around the GT line. The NOR logic monitors the Output B ratio at the following time states for Input *A* and Input *B* where *T* represents the typical time where PL is collected after excitation: (0,0) 0 μs; (1,0) 10 μs after *T*; (0,1) 20 μs after *T*; and (1,1) 30 μs after $2 \times T$ while the NAND logic monitors the output at the following time states: (0,0) 0 μs; (1,0) 10 μs before *T*; (0,1) at *T*; and (1,1) 10 μs before $2 \times T$. The Output B ratio utilized in both logic gates is converted into the Boolean Logic state of "ON or "1" for ratios greater than 2 and into "OFF" or "0" for ratios less than 2. Using, for example, $T = 70$ μs and a valence of 8 A647/QD, the initial state (0,0) will be measured immediately (no delay or 0 μs on the time axis) and produce an "ON" signal (within the blue area). Input *A* (1,0) will be measured after $70 + 10 = 80$ μs delay for NOR leading to an "OFF" signal (white area) and after $70 - 10 = 60$ μs delay for NAND leading to an "ON" signal (blue area). Input *B* (0,1) will be measured after $70 + 20 = 90$ μs delay for NOR leading to an "OFF" signal (white area) and after 70 μs (*T*) delay for NAND leading to an "ON" signal (on the GT line = blue area) in Fig. 5b. Continuing with this, Input $A + B$ (1,1) will be measured after $2 \times 70 + 30 = 170$ μs delay for NOR leading to an "OFF" signal (white area) and after $2 \times 70 - 10 = 130$ μs delay for NAND leading to an "OFF" signal (white area); note – the full range of the latter points are not shown in Fig. 5b. By analyzing more time points for *T* within the Tb-QD-A647 system with 12 Tb and 8 A647, we see how the creation of NOR and NAND gates can be produced at distinct time delays *T* (*i.e.*, 50 μs, 60 μs, 70 μs, and 100 μs) and then transition around a gate as noted by the NOR (blue) and NAND (light blue) icons in Fig. 5a.

Set-reset functionality with logic regeneration

Moving beyond the previous examples which were essentially static in nature in terms of the QD architecture itself, we set out to test this device architecture in a more dynamic or "active" biocomputing configuration while simultaneously addressing an issue that remains functionally challenging for most biologically based MLDs. A major drawback to current MLD design is the inability to reset the logic to the initial state—a function that permits information storage in a manner analogous to a write-read-erasable form.[68,69] We thus chose to regenerate distinct logic inputs of the previously assembled Tb-QD-A647 system *within the same samples* to verify the set-reset capability of our QD-based biophotonic logic devices, see Fig. 6 and the Experimental Section for a schematic and notes regarding the process. In this experiment, we focused on regenerating Input *B* or A647. Our strategy was as follows: (1) assemble a logic gate as before with the requisite ratios of PEP A-A647 and PEP B-Tb (Fig. 6a and b); (2) use a proteolytic enzyme to specifically cleave PEP A-A647 without perturbing PEP B-Tb, the A647 dye-label subsequently diffuses away from the QD preventing efficient FRET and altering that critical component of the resulting PL spectra and gate (Fig. 6c); (3) add a potent inhibitor to inactivate the enzyme (Fig. 6d); (4) reintroduce appropriate amounts of PEP A-A647 to the test vial to regenerate the logic gate (Fig. 6d); (5) repeat the process sequentially within the same sample tube as needed (Fig. 6e and f). Six logic state configurations consisting of 4 or 12 PEP B-Tb conjugated to a central QD with PEP A-A647 valences of 4, 6, 10 or 8, 10, and 18, respectively, were interrogated during these regeneration cycles.

Regeneration cycles were realized by using the addition of trypsin, a prototypical serine protease that cleaves PEP A which links the A647 to the QD and specifically hydrolyzes the bond C-terminal to the one arginine (R) residue.[70] PEP B, which connects the Tb to the central QD, contains no lysine or arginine residues and thus addition of trypsin removes the A647 from proximity to the QD through proteolytic activity while having no digestive effect on Tb-QD binding. After acquiring the regenerated PL intensity spectra at 20 min after trypsin injection (Fig. 6c and Experimental Section) an equimolar amount of soybean trypsin inhibitor was added to each test vial to neutralize the effects of trypsin and permit A647-QD rebinding. This inhibitor is a 181 residue polypeptide which forms a 1 : 1 stoichiometric complex with trypsin's active site. Following a 15 min time elapse from inhibitor injection, more A647 dye was subsequently added to each vial to create Tb-QD-A647 conjugates (valence = 6 A647) (Fig. 6d and Experimental Section). The second regeneration cycle was performed in a manner identical to the first, except for the use of a valence of 10 PEP A-A647, and again yielded regenerated PL spectra (Fig. 6e and f). The PL emission collected intermittently throughout the process reflects spectra reporting the presence or absence of A647 on the Tb-QD conjugates.

The corresponding emission PL ratios acquired immediately and after a 55 μs time delay from UV excitation (400 and 339 nm,

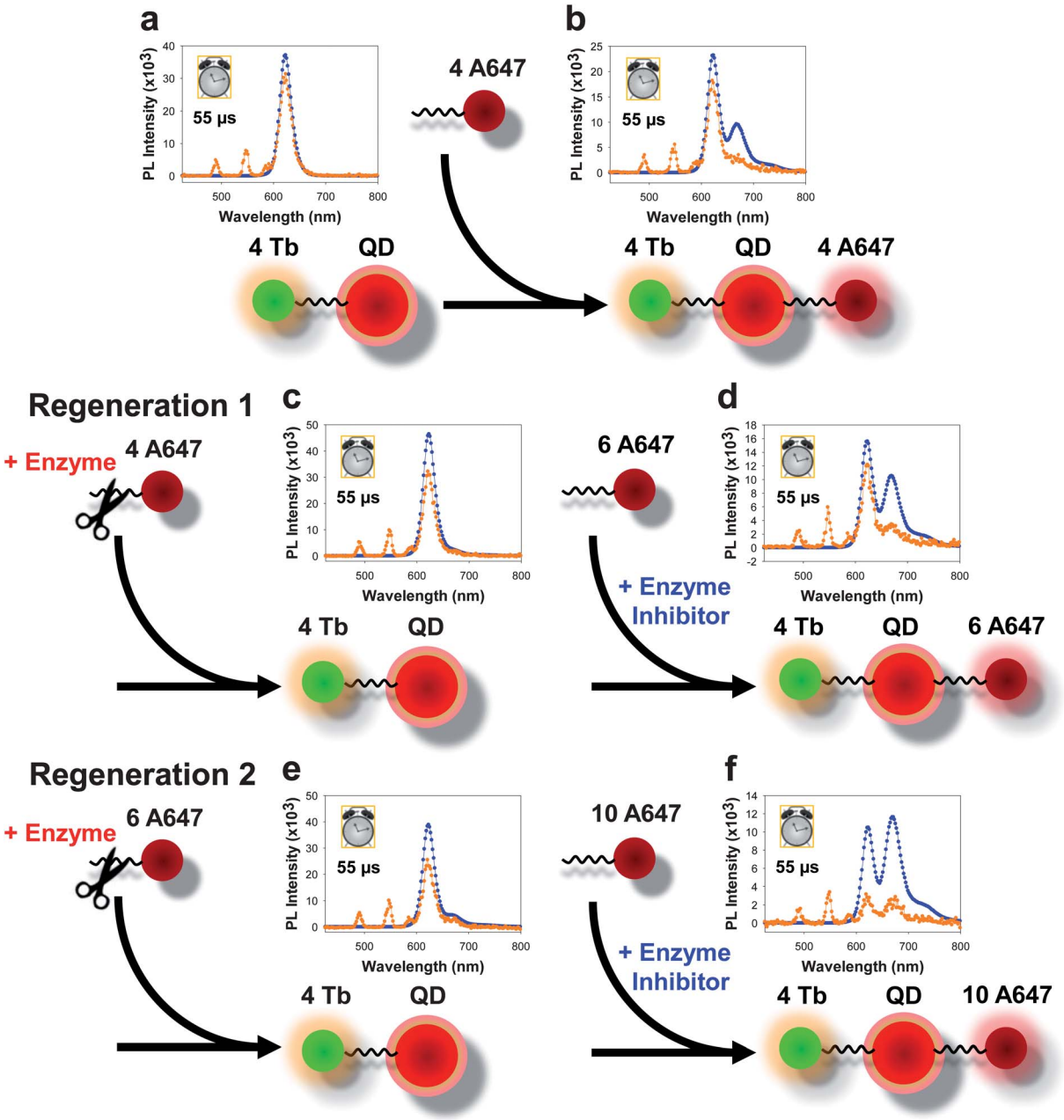

Fig. 6 Intermittent regeneration cycles for potential set-reset functionality shown schematically with the Tb-QD-A647 three-fluorophore system. PL plots display the output PL intensity immediately (blue) and 55 µs (orange) after 400 or 339 nm UV excitation, respectively. The spectra coding for the six total states with intermittent regeneration are shown as follows: (a) 4 Tb to QD and no A647; (b) 4 Tb to QD and 4 A647; (c) 4 Tb to QD, first regeneration cycle by sequential addition of trypsin (1 µL of 106 µM) that cleaves PEP A-A647 followed by addition of soybean trypsin inhibitor; (d) 4 Tb to QD and 6 A647; (e) 4 Tb to QD, second regeneration cycle; and (f) 4 Tb to QD and 10 A647.

respectively) are shown in Fig. 7a. The regeneration of each logic input was performed side-by-side in triplicate, which allowed each logic state to be repeated six times (see Experimental Section) and provided PL intensity ratio means and standard deviations for all PL output data. The error bars in these graphs show one standard deviation above and below these mean values. These graphs provide us with insight in how to choose Tb and A647 valences so output PL emissions yield statistically consistent Boolean logic "ON" and "OFF" values, especially after being implemented repeatedly with a regeneration step. For example, from the prompt PL intensity ratio displayed in Fig. 7a (Output A, blue column bars), the logic states with 4 or 12 Tb and 10 A647 assembled to a central QD could yield a value of "ON" or "OFF" as the standard deviation error bars extend below and above the threshold PL Intensity Ratio of 1. Thus, these logic input states could yield false positives or false negatives that would create inconsistent logic gates. However, input states containing 4 Tb and 4 A647 or 12 Tb and 18 A647 conjugated around a central QD would yield statistically consistent Boolean logic values of "OFF" and "ON", below or above the threshold PL Intensity Ratio of 1,

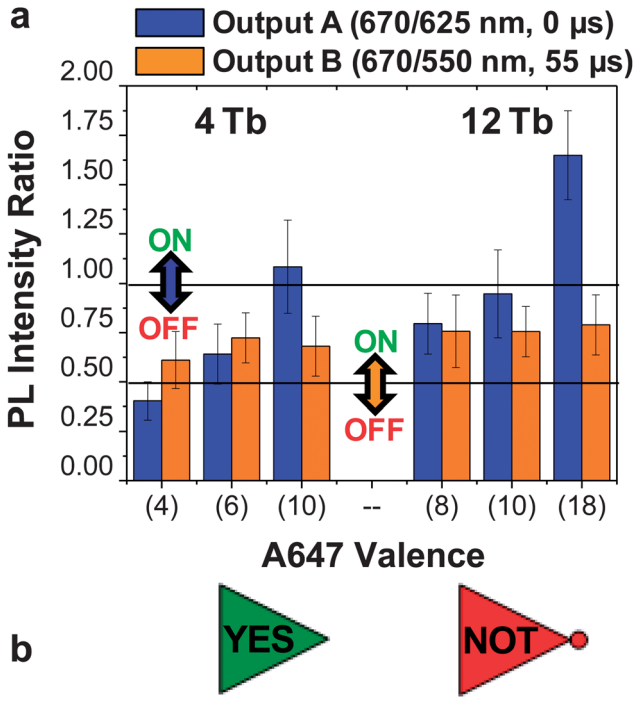

b

Input	Output PL	Output PL
	YES	NOT
0	0	0
1	1	0

Fig. 7 (a) The resultant peak PL intensity ratios for the Tb-QD-A647 three-fluorophore system with PEB-Tb valences of 4 and 12 and corresponding PEP A-A647 valences of 4,6,10 and 8,10,18, respectively (described in Fig. 6). PL intensity ratio of the A647 (670 nm) and the QD (625 nm) acquired (Output A-blue) immediately after 400 nm UV excitation and the ratio of A647 (670 nm) and the Tb (550 nm) acquired with 55 μs time delay after 339 nm UV excitation (Output B-orange). For immediate monitoring, the ratio above 1 is converted into the Boolean Logic state of "ON or 1" and ratios below 1 are "OFF or 0"; the analogous values used for the time-gated data are with 0.5. (b) This yields the truth table for single input, single output YES and NOT logic gates. Error bars portray standard deviation for 6 distinct trials ($n = 6$).

respectively, for Output A and would accordingly help create consistent logic gates (Fig. 1a).

Interestingly, without requiring any further modification, these individual logic input states could be used to create simple Yes/No (*i.e.*, YES and NOT logic gates) or single input, single output logic (Fig. 1b). In Yes/No logic, the absence and presence of Tb and A647 would yield the two input states of the YES and NOT logic gates with the output once again being derived from the appropriate PL intensity ratio plots. For example, an input state containing 4 Tb and 4 A647 conjugated to a central QD would yield a NOT gate while 12 Tb and 18 A647 conjugated to a central QD would yield a YES gate when PL emission was monitored immediately after 400 nm UV excitation, see Output A in Fig. 7b. A similar logic gate configuration can be applied to the corresponding time-delayed data.

Conclusions

To understand the value of the logic elements presented here, it is helpful to consider specific scenarios for which such MLDs are being developed. The Katz and Willner research groups pioneered sophisticated logic with enzyme-based gates (*e.g.*, OR, AND, INH gates, as well as half-adder and half-subtractor circuits) to follow and transduce metabolic processes or establish the effectiveness of drug delivery.[25,71,72] More recently, Katz teamed with Wang to diagnose injury states with enzyme-based logic (AND/IDENTITY gates); such devices have excellent potential for rapid diagnostics in remote locations (*e.g.*, warfighters in a battlefield).[73,74] In an alternate format, the de Silva group utilized MLDs as molecular computational identification (MCID) nanometric tags, inspired by the widely used radio-frequency identification (RFID) tags, to track small objects in large populations by observing the fluorescence from 0.1 mm polymer tracking beads with five distinguishable forms of logic (*i.e.*, YES, PASS 1, NOT, PASS 0 and PASS 1 + YES).[75] Kolpashchikov and Stojanovic built upon the ideas of logic operated oligonucleotide release first established by Shapiro and coworkers[19] to create AND and NAND gates from fluorescently tagged aptamers that could elicit a specific response by triggering drug delivery when oligonucleotide disease markers are expressed.[76]

There are many inherent advantages to our unimolecular QD-based logic gates, including the facile self-assembly chemistry, amenability to being easily incorporated into specific biosensing assays, potential for regeneration, wealth of available signals in real-time or time-delayed modality, multi-logic capabilities from single QD platforms, reconfigurable logic, flexibility in the excitation wavelengths such that one of the inputs can be turned off (*i.e.*, using 400 nm which completely excludes the Tb but still allows for QD excitation), and access to strong signal and resilience to photobleaching. Cumulatively, these advantages are well suited to augmenting MLD technologies. For example, the inputs of Tb and A647 could be associated with two different peptide or DNA sequences targeting different biological activity or markers for various biosensing applications. In particular, we envision bioconjugating Tb or A647 to the central QD logic platform *via* a unique enzyme recognized peptide cleavage sequence (*e.g.*, DEVD) that can be cleaved by an activated proteolytic enzyme (*e.g.*, caspase 3).[77] Caspase-catalyzed cleavage of A647 and/or Tb from the central QD would change the overall photonic logic and therefore could be used to monitor molecules that activate caspase enzymes as part of the pathways initiated during apoptosis or programmed cell death, which is associated with diseases such as cancer and Alzheimer's disease.[78,79] Continuing with the targeting of proteases, other proteolytic processes that are critical to thrombolytic diseases and injury (*i.e.*, blood clotting) could be monitored in a similar fashion.[80] When used alone or in conjunction with other biomolecular logic platforms (*e.g.*, oligonucleotides or enzymes), these QD-based logic gates could potentially be useful for small chemical/biomolecular identification as part of a theranostic device. The complexity inherent to these devices suggests that they can provide information far

beyond a simple Yes/No diagnostic format. Indeed, given the ratiometric basis for most of the logic highlighted here, data may be available on the relative activity of particular biomolecular processes such as the level or stage of blood clotting, for example. Drug release could be facilitated concomitant with sensing by having the drug attached to a peptide that is similarly responsive and cleaved by the protease of interest. Furthermore, the excellent 2-photon and FRET capabilities of QDs in general suggest the possibility of direct *in situ* cellular or tissue monitoring.[81] Alternatively, combining Tb with QDs and collecting PL in a time-delayed mode can provide similar deep tissue *in vivo* access as the strong fluorescent background of biological media such as blood can be overcome.[82] The excellent multiplexing suitability of Tb and QD-based FRET systems[83,84] further suggests that simultaneous use of multiple differentially colored photonic gates within a single sample is also possible.

In summary, the concentric coassembly of peptides labeled with Tb and A647 around a central QD was used to develop a nanoplatform capable of creating multiple logic expressions. These core components had previously been utilized for biosensing and here we expand on their potential and demonstrate signal-rich unimolecular biophotonic logic gates that are capable of performing single output Boolean logic including OR, AND, INHIBIT, XOR, NOR, and NAND functions. Ratiometric assembly and the capacity to incorporate multistep FRET processes was the key to developing such a multi-logic supramolecule. The facile molecular assembly configuration utilized here overcomes complex photonic MLD fabrication techniques (*e.g.* ss-DNA strand invasion, dye irradiation/excitation at multiple wavelengths, conformational changes in hairpin DNA probes, and threading/unthreading of molecular machines) that have hindered photonic MLD design, complexity, and potential applicability to real world applications. Furthermore, the set-reset nature of the Tb-QD-A647 system with logic state reconfiguration opens up the system to far more complex logic and implementation in a format where operations are repeated over time, thus adding to and expanding the current repertoire of available biophotonic MLD's.[85,86] This set-reset function also demonstrates the ability to potentially access information in a write-read-erasable format as found in most electronic storage devices, paving the way for reconfigurable logic where chemical manipulation can be used to created distinct logic expressions from the same molecule/supramolecule.[87]

Experimental section

Materials

The 625 nm emitting QDs were kindly provided by Invitrogen Life Technologies (Eugene, OR). These were modified with PEG-appended dihydrolipoic acid as described.[88] Peptides CSTRTDEGNQGGTSSP$_7$SH$_6$ and GSGAAAGLSH$_6$ were obtained from Biosynthesis, Inc. (Lewisville, TX). Alexa Fluor 647-maleimide was obtained from Invitrogen Life Technologies and *N*-hydroxysuccinimide ester Lumi4®-Tb from Lumiphore (Richmond, CA).[89] Phosphate buffered saline (PBS, 10 mM phosphate, 137 mM NaCl, 3 mM KCl, pH 7.4), trypsin (from bovine pancreas, MW ~ 24 kDa, 10 000 BAEE units per mg), and soybean trypsin inhibitor were all obtained from Sigma (St Louis, MO). 96-well black polystyrene non-binding surface microtiter plates were obtained from Corning.

Relevant photophysical properties and spectral data acquisition

Fluorophore photophysical properties. Tb: $\lambda_{abs.max}$ 339 nm; ε_{max} 26 000 M^{-1} cm^{-1}; $\lambda_{em.}$ ~ 490, 550, 585, and 620 nm; Q.Y. ~0.60 for the overall complex and ~0.77 for the central Tb-ion. QD: ε_{610nm} 5.5 × 10^5 M^{-1} cm^{-1}, $\lambda_{em.max}$ 625 nm, Q.Y. ~0.60. A647: $\lambda_{abs.max}$ 650 nm; ε_{max} 89 000 M^{-1} cm^{-1}; $\lambda_{em.max}$ 670 nm Q.Y. ~0.33. Förster distances (R_0): Tb → QD = 10.1 nm, QD → A647 = 7.5 nm.[54] Spectra were collected on a Tecan Infinite M1000 dual monochromator multifunction plate reader equipped with a xenon flash lamp (Tecan, Research Triangle Park, NC). Immediate spectra acquisition: 400 Hz flash frequency, 400 nm excitation, ~0 μs delay between flash and data acquisition, and a 40 μs integration time. Time-delayed spectra acquisition: 100 Hz flash frequency, 339 nm excitation, 55 μs delay, 1 ms integration time or as specifically indicated in the text.[54,55] Note, the photophysical properties of these materials are quite complex and so the spectra and their relative intensities and cross-contributions may vary depending upon the collection instrument and settings used.[54,55] In particular, some of the changes in time-gated PL intensity signals over tens of microseconds are tentatively attributed, at least in part, to aftereffects of intense immediate QD PL on the time-gated detection.

Peptide labeling and purification

Peptide CSTRTDEGNQGGTSSP$_7$SH$_6$ was labeled at the *N*-terminal cysteine residue with A647-maleimide and peptide GSGAAAGLSH$_6$ was labeled with an *N*-hydroxysuccinimide ester Lumi4®-Tb at its *N*-terminus to yield PEP A-A647 and PEP B-Tb, respectively, using the methods described in detail previously.[88] Briefly, for the maleimide coupling to the cysteine on PEP A, approximately 1 mg of peptide (in the trifluoroacetic acid salt form) was added in 1 mL of 10× PBS to a large excess of Alexa Fluor 647-maleimide dye and agitated for 16 hours at 4 °C. The His$_6$-labeled peptide was then captured on three consecutive 1 mL columns of Ni^{2+}–nitrilotriacetic acid agarose media (Qiagen) and washed copiously with excess 1× PBS. Labeled peptide was eluted with 300 mM imidazole in 1× PBS. A reverse-phase oligonucleotide purification cartridge (OPC, Applied Biosystems) was then used to remove the imidazole and desalt the Cy3-peptide. The OPC was prepared with 3 mL acetonitrile followed by 3 mL of 2 M triethylamine acetate (TEAA, Applied Biosystems). The labeled peptide was bound to the column, washed with excess 0.02 M TEAA and removed from the column using 70% acetonitrile in H_2O. The OPC was reused in the same manner for at least three more rounds of purification until no more labeled product was being eluted. The desalted peptide was quantitated by UV-vis spectroscopy, aliquoted and lyophilized for storage at −20 °C in a dessicator until required in experiments. The PEP B-Tb was prepared in a similar manner with adjustments to the buffer composition to optimize the pH for the amine-reactive chemistry and preserve the Tb complex (no phosphate).[54,90]

Table 1 Volumes and equivalents used for the set-reset logic regeneration[a]

Input cycle	4 Tb	4 Tb	4 Tb	12 Tb	12 Tb	12 Tb
1	2 μL (4 A647)	3 μL (6 A647)	5 μL (10 A647)	4 μL (8 A647)	5 μL (10 A647)	9 μL (18 A647)
2	3 μL (6 A647)	5 μL (10 A647)	2 μL (4 A647)	5 μL (10 A647)	9 μL (18 A647)	4 μL (8 A647)
3	5 μL (10 A647)	2 μL (4 A647)	3 μL (6 A647)	9 μL (18 A647)	4 μL (8 A647)	5 μL (10 A647)

[a] Each sample was regenerated from top of the column down and order of regeneration was varied to evaluate repeatability.

Assembly of Tb-QD-A647 logic devices

The QD assembly with peptide conjugates were usually prepared at 45 nM by adding 5 pmol of QD stock to a prediluted solution of the desired equivalents of Tb-peptide and A647-peptide in PBS buffer to yield a final volume of *ca.* 100–110 μL. The concentration of Tb-peptide and A647-peptide were varied to yield the desired Tb to QD and A647 to QD valences for distinct inputs (*e.g.*, Input *A* and Input *B*) in logic gate formation. These solutions were allowed to equilibrate at room temperature for at least 1–2 h prior to collecting PL measurements.

Logic regeneration procedure

This assay is based on using stock solutions of 1 μM QD, and 10 μM of PEP A-A647 and PEP B-Tb each. To recreate the logic states with 4 Tb assembled to the central QD, add 2.0 μL PEP B-Tb to 103 μL PBS with 5.0 μL QD (Table 1). To recreate the logic states with 12 Tb assembled to a central QD, add 6.0 μL of PEP B-Tb to 99.0 μL PBS with 5.0 μL of QD (Table 1). In each case, mix in Eppendorf tubes and let the QD-Tb conjugates stand for ~60 min. Transfer to the microtiter plate and acquire initial spectra. Transfer samples back to Eppendorf tubes and add Input 1 (Table 1). Let stand ~30 min and transfer to microtiter plate. Acquire "Input 1" spectra. Add to 1 μL of 106 μM trypsin and track digestion (using A647/QD PL) over 20 min to confirm digestion complete. Acquire spectra corresponding to "Regeneration 1." Add 4 μL of 43 μM soybean trypsin inhibitor. Transfer to Eppendorf tubes. Let stand 15 min. Add Input 2 (Table 1). Let stand ~30 min and transfer to plate to acquire spectra ("Input 2"). Add 6 μL of 106 μM trypsin solution. Again track digestion (using A647/QD PL) over 20 min to confirm digestion complete. Acquire spectrum corresponding to "Regeneration 2." Add 25 μL of 43 μM soybean trypsin indicator (STI) and transfer to Eppendorf tubes for 15 min. Add Input 3 (Table 1) and let stand ~30 min. Acquire spectrum corresponding to "Input 3." Each triplicate experiment was performed at least twice to confirm the data.

Acknowledgements

The authors acknowledge NRL, NRL NSI, ONR, DARPA, DTRA-JSTO MIPR no. B112582M, the European Commission (FP7 project Nanognostics), the University of British Columbia, a Canada Research Chair (Tier 2, WRA) and the Canada Foundation for Innovation (CFI) for financial support. The authors thank Lumiphore, Inc. for the Lumi4-Tb reagents and Invitrogen Life Sciences for the QDs.

References

1 C. P. Collier, E. W. Wong, M. Belohradsky, F. M. Raymo, J. F. Stoddart, P. J. Kuekes, R. S. Williams and J. R. Heath, *Science*, 1999, **285**, 391.
2 A. P. de Silva and S. Uchiyama, *Nat. Nanotechnol.*, 2007, **2**, 399.
3 R. J. Amir, M. Popkov, A. R. Lerner, C. F. Barbas and D. Shabat, *Angew. Chem., Int. Ed.*, 2005, **117**, 4452.
4 M. Hammarson, J. Andersson, S. Li, P. Lincoln and J. Andréasson, *Chem. Commun.*, 2010, **46**, 7130.
5 M. Privman, T. K. Tam, V. Bocharova, J. Halámek, J. Wang and E. Katz, *ACS Appl. Mater. Interfaces*, 2011, **3**, 1620.
6 O. A. Bozdemir, R. Guliyev, O. Buyukcakir, S. Selcuk, S. Kolemen, G. Gulseren, T. Nalbantoglu, H. Boyaci and E. U. Akkaya, *J. Am. Chem. Soc.*, 2010, **132**, 8029.
7 M. Elstner, K. Weisshart, K. Mullen and A. Schiller, *J. Am. Chem. Soc.*, 2012, **134**, 8098.
8 N. Kaur, N. Singh, D. Cairns and J. F. Callan, *Org. Lett.*, 2009, **11**, 2229.
9 J. J. Lavigne and E. V. Anslyn, *Angew. Chem., Int. Ed.*, 2001, **40**, 3118.
10 G. J. Brown, A. P. de Silva, M. R. James, B. O. F. McKinney, D. A. Pears and S. M. Weir, *Tetrahedron*, 2006, **64**, 8301.
11 T. Konry and D. R. Walt, *J. Am. Chem. Soc.*, 2009, **131**, 13232.
12 D. Margulies and A. D. Hamilton, *J. Am. Chem. Soc.*, 2009, **131**, 9142.
13 S. Angelos, Y. W. Yang, N. M. Khashab, J. F. Stoddart and J. I. Zink, *J. Am. Chem. Soc.*, 2009, **131**, 11344.
14 S. M. Douglas, I. Bachelet and G. M. Church, *Sci. Signaling*, 2012, **335**, 831.
15 J. Elbaz and I. Willner, *Nat. Mater.*, 2012, **11**, 276.
16 M. Motornov, J. Zhou, M. Pita, V. Gopishetty, I. Tokarev, E. Katz and S. Minko, *Nano Lett.*, 2008, **8**, 2993.
17 M. B. Elowitz and S. Leibler, *Nature*, 2000, **403**, 335.
18 T. S. Gardner, C. R. Cantor and J. J. Collins, *Nature*, 2000, **403**, 339.
19 Y. Benenson, B. Gil, U. Ben-Dor, R. Adar and E. Shapiro, *Nature*, 2004, **429**, 423.
20 Y. Fu, X. Hu, C. Lu, S. Yue, H. Yang and Q. Gong, *Nano Lett.*, 2012, **12**, 5784.
21 X. Liu, R. Aizen, R. Freeman, O. Yehezkeli and I. Willner, *ACS Nano*, 2012, **6**, 3553.
22 A. Saghatelian, N. H. Volcker, K. M. Guckian, V. S.-Y. Lin and M. R. Ghadiri, *J. Am. Chem. Soc.*, 2002, **125**, 346.
23 J. Andréasson, D. Stephen, G. Kodis, P. Choong-Do, M. Hambourger, M. Gervaldo, B. Albinsson, T. A. Moore, A. L. Moore and D. Gust, *J. Am. Chem. Soc.*, 2006, **128**, 16259.

24 S. Auslander, D. Auslander, M. Muller, M. Wieland and M. Fussenegger, *Nature*, 2012, **487**, 123.
25 R. Baron, O. Lioubashevski, E. Katz, T. Niazov and I. Willner, *J. Phys. Chem. A*, 2006, **110**, 8548.
26 S. J. Langford and T. Yann, *J. Am. Chem. Soc.*, 2003, **125**, 11198.
27 D. H. Qu, Q. C. Wang and H. Tian, *Angew. Chem., Int. Ed.*, 2005, **44**, 5296.
28 R. Baron, O. Lioubashevski, E. Katz, T. Niazov and I. Willner, *Angew. Chem., Int. Ed.*, 2006, **118**, 1602.
29 Y. Liu, A. Offenhäusser and D. Mayer, *Angew. Chem., Int. Ed.*, 2010, **49**, 2595.
30 M. N. Stojanovic, S. Semova, D. Kolpashchikov, J. Macdonald, C. Morgan and D. J. Stefanovic, *J. Am. Chem. Soc.*, 2005, **127**, 6914.
31 P. A. de Silva, N. H. Q. Gunaratne and C. P. McCoy, *Nature*, 1993, **364**, 42.
32 S. J. Langford and T. J. Yann, *J. Am. Chem. Soc.*, 2003, **125**, 11198.
33 J. Andréasson, U. Pischel, S. D. Straight, T. A. Moore, A. L. Moore and D. Gust, *J. Am. Chem. Soc.*, 2011, **133**, 11641.
34 A. P. de Silva, I. M. Dixon, H. Q. Nimal Gunaratne, T. Gunnlaugsson, P. R. S. Maxwell and T. E. Rice, *J. Am. Chem. Soc.*, 1999, **121**, 1393.
35 D. Gust, T. A. Moore and A. L. Moore, *Chem. Commun.*, 2006, 1169.
36 P. Remon, M. Balter, S. Li, J. Andréasson and U. Pischel, *J. Am. Chem. Soc.*, 2011, **133**, 20742.
37 Y. Zhai, Z. Zhu, C. Zhu, J. Zhu, J. Zhu, J. Ren, E. Wang and S. Dong, *Nanoscale*, 2013, **5**, 4344.
38 J. Li, X. Jia, D. Li, J. Ren, Y. Han, Y. Xia and E. Wang, *Nanoscale*, 2013, **5**, 6131.
39 C. W. Lien, Y. C. Chen, H. T. Chang and C. C. Huang, *Nanoscale*, 2013, **5**, 8227.
40 E. Busseron, Y. Ruff, E. Moulin and N. Giuseppone, *Nanoscale*, 2013, **5**, 7098.
41 S. Gaweda, A. Podborska, W. Macyk and K. Szacilowski, *Nanoscale*, 2009, **1**, 299.
42 Y. Li, H. Zheng, Y. Li, S. Wang, Z. Wu, P. Liu, Z. Gao, H. Liu and D. J. Zhu, *J. Org. Chem.*, 2007, **72**, 2878.
43 K. J. Herbst, Q. Ni and J. Zhang, *IUBMB Life*, 2009, **61**, 902.
44 S. Zadran, S. Standley, K. Wong, E. Otiniano, A. Amighi and M. Baudry, *Appl. Microbiol. Biotechnol.*, 2012, **96**, 2012.
45 C. Pistol, C. Dwyer and A. R. Lebeck, *IEEE Micro*, 2008, **28**, 7.
46 S. Buckhout-White, M. Ancona, E. Oh, J. R. Deschamps, M. H. Stewart, J. B. Blanco-Canosa, P. E. Dawson, E. R. Goldman and I. L. Medintz, *ACS Nano*, 2012, **6**, 1026.
47 E. Graugnard, D. L. Kellis, H. Bui, S. Barnes, W. Kuang, J. Lee, W. L. Hughes, W. B. Knowlton and B. Yurke, *Nano Lett.*, 2012, **12**, 2117.
48 K. S. Park, M. W. Seo, C. Jung, J. Y. Lee and H. G. Park, *Small*, 2012, **8**, 2203.
49 B. Yurke, A. J. Turberfield, A. P. Mills, F. C. Simmel and J. L. Neumann, *Nature*, 2000, **406**, 605.
50 I. L. Medintz and H. Mattoussi, *Phys. Chem. Chem. Phys.*, 2009, **11**, 17.
51 W. R. Algar, K. Susumu, J. B. Delehanty and I. L. Medintz, *Anal. Chem.*, 2011, **83**, 8826.
52 K. E. Sapsford, L. Berti and I. L. Medintz, *Angew. Chem., Int. Ed.*, 2006, **45**, 4562.
53 U. O. S. Seker, E. Mutlugun, P. L. Hernandez-Martinez, V. K. Sharma, V. Lesnyak, N. Gaponik, A. Eychmüller and H. V. Demir, *Nanoscale*, 2013, **5**, 7034.
54 W. R. Algar, D. Wegner, A. L. Huston, J. B. Blanco-Canosa, M. H. Stewart, A. Armstrong, P. E. Dawson, N. Hildebrandt and I. L. Medintz, *J. Am. Chem. Soc.*, 2012, **134**, 1876.
55 W. R. Algar, A. P. Malanoski, K. Susumu, M. H. Stewart, N. Hildebrandt and I. L. Medintz, *Anal. Chem.*, 2012, **84**, 10136.
56 J. Andréaasson and D. Gust, *Photonically Switched Molecular Logic Devices*, Wiley-VCH, Weinheim, 2012, p. 53.
57 A. P. de Silva, *Molecular Logic-Based Computation*, Royal Society of Chemistry, Cambridge, 2012, p. 397.
58 K. E. Sapsford, T. Pons, I. L. Medintz, S. Higashiya, F. M. Brunel, P. E. Dawson and H. Mattoussi, *J. Phys. Chem. C*, 2007, **111**, 11528.
59 K. E. Sapsford, W. R. Algar, L. Berti, K. B. Gemmill, B. J. Casey, E. Oh, M. H. Stewart and I. L. Medintz, *Chem. Rev.*, 2013, **11**, 1904.
60 W. R. Algar, D. E. Prasuhn, M. H. Stewart, T. L. Jennings, J. B. Blanco-Canosa, P. E. Dawson and I. L. Medintz, *Bioconjugate Chem.*, 2011, **22**, 825.
61 D. E. Prasuhn, J. R. Deschamps, K. Susumu, M. H. Stewart, K. Boeneman, J. B. Blanco-Canosa, P. E. Dawson and I. L. Medintz, *Small*, 2010, **6**, 555.
62 L. J. Charbonniere and N. Hildebrandt, *Eur. J. Inorg. Chem.*, 2008, **2008**, 324.
63 Y. Liu, A. Offenhäusser and D. Mayer, *Angew. Chem., Int. Ed.*, 2010, **122**, 2649.
64 S. D. Straight, P. A. Liddell, Y. Terazono, T. A. Moore, A. L. Moore and D. Gust, *Adv. Funct. Mater.*, 2007, **17**, 777.
65 A. Credi, V. Balzani, S. J. Langford and J. F. Stoddart, *J. Am. Chem. Soc.*, 1997, **119**, 2679.
66 J. Andréasson, U. Pischel, S. D. Straight, T. A. Moore, A. L. Moore and D. Gust, *J. Am. Chem. Soc.*, 2011, **133**, 11641.
67 A. P. de Silva and N. D. McClenaghan, *Chem.–Eur. J.*, 2004, **10**, 574.
68 J. Elbaz, Z. G. Wang, R. Orbach and I. Willner, *Nano Lett.*, 2009, **9**, 4510.
69 D. Liu, W. Chen, K. Sun, K. Deng, W. Zhang, Z. Wang and X. Jiang, *Angew. Chem., Int. Ed.*, 2011, **50**, 4103.
70 K. E. Sapsford, J. Granek, J. R. Deschamps, K. Boeneman, J. B. Blanco-Canosa, P. E. Dawson, K. Susumu, M. H. Stewart and I. L. Medintz, *ACS Nano*, 2011, **5**, 2687.
71 R. Baron, O. Lioubashevski, E. Katz, T. Niazov and I. Willner, *Angew. Chem., Int. Ed.*, 2006, **118**, 1602.
72 T. Niazov, R. Baron, E. Katz, O. Lioubashevski and I. Willner, *Proc. Natl. Acad. Sci. U. S. A.*, 2006, **103**, 17160.

73 K. M. Manesh, J. Halámek, M. Pita, J. Zhou, T. K. Tam, P. Santhosh, M.-C. Chuang, J. R. Windmiller, D. Abidin and E. Katz, *Biosens. Bioelectron.*, 2009, **24**, 3569.
74 D. Melnikov, G. Strack, J. Zhou, J. R. Windmiller, J. Halámek, V. Bocharova, M.-C. Chuang, P. Santhosh, V. Privman and J. Wang, *J. Phys. Chem. B*, 2010, **114**, 12166.
75 A. P. De Silva, M. R. James, B. O. F. McKinney, D. A. Pears and S. M. Weir, *Nat. Mater.*, 2006, **5**, 787.
76 D. M. Kolpashchikov and M. N. Stojanovic, *J. Am. Chem. Soc.*, 2005, **127**, 11348.
77 K. Boeneman, B. C. Mei, A. M. Dennis, G. Bao, J. R. Deschamps, H. Mattoussi and I. L. Medintz, *J. Am. Chem. Soc.*, 2009, **131**, 3828.
78 R. Onuki, A. Nagasaki, H. Kawasaki, T. Baba, T. Q. P. Uyeda and K. Taira, *Proc. Natl. Acad. Sci. U. S. A.*, 2002, **99**, 14716.
79 J. Yuan and B. A. Yankner, *Nature*, 2000, **407**, 802.
80 S. R. J. Coughlin, *Thromb. Haemostasis*, 2005, **3**, 1800.
81 A. R. Clapp, T. Pons, I. L. Medintz, J. B. Delehanty, J. S. Melinger, T. Tiefenbrunn, P. E. Dawson, B. R. Fisher, B. O'Rourke and H. Mattoussi, *Adv. Mater.*, 2007, **19**, 1921.
82 F. Morgner, S. Stufler, D. Geißler, I. L. Medintz, W. R. Algar, K. Susumu, M. H. Stewart, J. B. Blanco-Canosa, P. E. Dawson and N. Hildebrandt, *Sensors*, 2011, **11**, 9667.
83 D. Geißler, L. J. Charbonnière, R. F. Ziessel, N. G. Butlin, H.-G. Löhmannsröben and N. Hildebrandt, *Angew. Chem., Int. Ed.*, 2010, **49**, 1396.
84 D. Geißler, S. Stufler, H.-G. Löhmannsröen and N. Hildebrandt, *J. Am. Chem. Soc.*, 2013, **135**, 1102.
85 D. Han, Z. Zhu, C. Wu, L. Peng, L. Zhou, B. Gulbakan, G. Zhu, K. Williams and W. Tan, *J. Am. Chem. Soc.*, 2012, **134**, 20797.
86 M.-C. Chuang, J. R. Windmiller, P. Santhosh, G. V. Ramírez, E. Katz and J. Wang, *Chem. Commun.*, 2011, **47**, 3087.
87 A. P. de Silva and N. D. McClenaghan, *Chem.–Eur. J.*, 2004, **10**, 574.
88 B. C. Mei, K. Susumu, I. L. Medintz and H. Mattoussi, *Nat. Protocols*, 2009, **4**, 412.
89 J. Xu, T. M. Corneillie, E. G. Moore, G.-L. Law, N. G. Butlin and K. N. Raymond, *J. Am. Chem. Soc.*, 2011, **133**, 19900.
90 K. E. Sapsford, D. Farrell, S. Sun, A. Rasooly, H. Mattoussi and I. L. Medintz, *Sens. Actuators, B*, 2009, **139**, 13.

